The Astrophysical Journal, 735:5 (12pp), 2011 July 1 doi:10.1088/0004-637X/735/1/5

HUBBLE SPACE TELESCOPE IMAGING OF Lyα EMISSION AT $z \approx 4.4$*

Steven L. Finkelstein[1], Seth H. Cohen[2], Rogier A. Windhorst[2], Russell E. Ryan[3], Nimish P. Hathi[4], Keely D. Finkelstein[1], Jay Anderson[5], Norman A. Grogin[5], Anton M. Koekemoer[5], Sangeeta Malhotra[2], Max Mutchler[5], James E. Rhoads[2], Patrick J. McCarthy[4], Robert W. O'Connell[6], Bruce Balick[7], Howard E. Bond[5], Daniela Calzetti[8], Michael J. Disney[9], Michael A. Dopita[10], Jay A. Frogel[11], Donald N. B. Hall[12], Jon A. Holtzman[13], Randy A. Kimble[14], Gerard Luppino[12], Francesco Paresce[15], Abhijit Saha[16], Joseph I. Silk[17], John T. Trauger[18], Alistair R. Walker[19], Bradley C. Whitmore[5], and Erick T. Young[20]

[1] George P. and Cynthia Woods Mitchell Institute for Fundamental Physics and Astronomy, Department of Physics & Astronomy, Texas A&M University, College Station, TX 77843, USA; stevenf@physics.tamu.edu
[2] School of Earth and Space Exploration, Arizona State University, Tempe, AZ 85287-1404, USA
[3] Department of Physics, University of California, Davis, CA 92616, USA
[4] Observatories of the Carnegie Institution of Washington, Pasadena, CA 91101, USA
[5] Space Telescope Science Institute, 3700 San Martin Drive, Baltimore, MD 21218, USA
[6] Department of Astronomy, University of Virginia, Charlottesville, VA 22904-4325, USA
[7] Department of Astronomy, University of Washington, Seattle, WA 98195-1580, USA
[8] Department of Astronomy, University of Massachusetts, Amherst, MA 01003, USA
[9] School of Physics and Astronomy, Cardiff University, Cardiff CF24 3AA, UK
[10] Research School of Astronomy & Astrophysics, The Australian National University, ACT 2611, Australia
[11] Association of Universities for Research in Astronomy, Washington, DC 20005, USA
[12] Institute for Astronomy, University of Hawaii, Honolulu, HI 96822, USA
[13] Department of Astronomy, New Mexico State University, Las Cruces, NM 88003, USA
[14] NASA-Goddard Space Flight Center, Greenbelt, MD 20771, USA
[15] Istituto di Astrofisica Spaziale e Fisica Cosmica, INAF, Via Gobetti 101, 40129 Bologna, Italy
[16] National Optical Astronomy Observatories, Tucson, AZ 85726-6732, USA
[17] Department of Physics, University of Oxford, Oxford OX1 3PU, UK
[18] NASA-Jet Propulsion Laboratory, Pasadena, CA 91109, USA
[19] Cerro Tololo Inter-American Observatory, La Serena, Chile
[20] NASA-Ames Research Center, Moffett Field, CA 94035, USA
Received 2010 August 3; accepted 2011 April 12; published 2011 June 7

ABSTRACT

We present the highest redshift detections of resolved Lyα emission, using *Hubble Space Telescope* (*HST*)/Advanced Camera for Surveys F658N narrowband-imaging data taken in parallel with the Wide Field Camera 3 Early Release Science program in the GOODS Chandra Deep Field-South. We detect Lyα emission from three spectroscopically confirmed $z = 4.4$ Lyα emitting galaxies (LAEs), more than doubling the sample of LAEs with resolved Lyα emission. Comparing the light distribution between the rest-frame ultraviolet continuum and narrowband images, we investigate the escape of Lyα photons at high redshift. While our data do not support a positional offset between the Lyα and rest-frame ultraviolet (UV) continuum emission, the half-light radius in one out of the three galaxies is significantly ($>1\sigma$) larger in Lyα than in the rest-frame UV continuum. Stacking the three LAEs in both the narrowband and UV continuum images, we find that the Lyα light appears larger than the rest-frame UV at 4.2σ significance. This Lyα flux detected with *HST* is a factor of 4–10 less than observed in similar filters from the ground. These results together imply that the Lyα emission is not strictly confined to its indigenous star-forming regions. Rather, for at least one object the Lyα emission is more extended, with the missing *HST* flux possibly existing in a diffuse outer halo. This suggests that the radiative transfer of Lyα photons in high-redshift LAEs is complicated, with the interstellar-medium geometry and/or outflows playing a significant role in galaxies at these redshifts.

Key words: galaxies: evolution – galaxies: high-redshift – galaxies: ISM

Online-only material: color figures

1. INTRODUCTION

High-redshift Lyα emitting galaxies (LAEs) are some of the most intriguing objects in the distant universe. Their strong Lyα emission was thought to be indicative of the first galaxies (Partridge & Peebles 1967), implying that they could possibly contain the first stars and likely be composed of pristine gas. However, recent studies of their physical properties imply that some of these galaxies may be more evolved, with many LAEs exhibiting rest-frame ultraviolet colors indicative of modest-to-moderate dust extinction (e.g., Pirzkal et al. 2007; Lai et al. 2007; Finkelstein et al. 2008, 2009b; Pentericci et al. 2009; Nilsson & Møller 2009; Ono et al. 2010). As Lyα photons are resonantly scattered by neutral hydrogen, galaxies with dust would be unlikely to exhibit Lyα in emission. Thus, just how Lyα escapes from a galaxy with a dusty interstellar medium (ISM) is an outstanding question in the study of distant galaxies.

As LAEs have been selected on the basis of their Lyα emission, some mechanism must allow the escape of these

* Based on observations made with the NASA/ESA *Hubble Space Telescope*, obtained at the Space Telescope Science Institute, which is operated by the Association of Universities for Research in Astronomy, Inc., under NASA contract NAS 5-26555. These observations are associated with program no. 11359.

photons. One possibility is that the Lyα photons we see have been shifted out of resonance by scattering off the receding edge of an outflow in the ISM. Evidence for outflows has been observed many times in the typically more evolved Lyman break galaxies (LBGs; e.g., Shapley et al. 2003; Bielby et al. 2010) as a velocity difference between Lyα emission and ISM absorption features. Only recently have outflows been shown to exist in LAEs. McLinden et al. (2010) discovered that in two LAEs at $z \sim 3.1$ Lyα emission had a slightly higher redshift than the rest-frame optical [O III] emission, which is thought to come from H II regions at the systemic redshift. Finkelstein et al. (2011) found that one of two $z \sim 2.3$ LAEs with detected Hα and [O III] emission showed a similar velocity offset from Lyα. In these cases, much of the Lyα emission is shifted redward of the resonance line at 1216 Å, and thus will have an easier chance of escaping, even in a uniform ISM.

Alternatively, if the line emission is primarily at resonance, much of the Lyα emission can still escape if the ISM is primarily clumpy, as the Lyα photons will scatter off the clumps, and be screened from seeing much of the dust (Neufeld 1991; Hansen & Oh 2006). This type of ISM geometry can explain the dustiness of LAEs at $z \sim 4.5$ (Finkelstein et al. 2008, 2009b), and can also explain the large number of high Lyα equivalent widths (EWs) which have been observed (e.g., Kudritzki et al. 2000; Malhotra & Rhoads 2002; Finkelstein et al. 2007). It can also explain the observed Lyα emission seen from extremely dusty galaxies such as ultra-luminous infrared galaxies (ULIRGs) and submillimeter galaxies (SMGs) at high redshift (e.g., Nilsson & Møller 2009; Capak et al. 2008).

In either of these radiative-transfer scenarios, any detected Lyα emission will be spatially decorrelated from its origination point within its host galaxy. Using radiative-transfer modeling, Zheng et al. (2010) find that spatial diffusion of Lyα photons results in extended Lyα emission from an intrinsic Lyα point source. This Lyα halo extends into the intergalactic medium, merging with those from other galaxies to create a Lyα background. By comparing Lyα emission from a narrowband filter to the rest-frame UV emission from a neighboring broadband filter, one can diagnose whether this is the case; if Lyα has undergone any extreme radiative-transfer effects, this should reveal itself in a larger size in the Lyα emission, as well as possibly a diffuse Lyα halo. This can be difficult at cosmological distances, as the derived Lyα size depends on the surface-brightness limit of the imaging. Locally, Östlin et al. (2009) have studied a sample of starburst galaxies and found that the bulk of Lyα photons emerge in a diffuse component resulting from resonant scattering. They also see radical changes from absorption to emission on very small scales, implying that Lya also escapes through favorable paths in a porous and inhomogeneous ISM.

Thus, studying the spatial distribution at high redshift is of interest, to examine whether the bulk of the Lyα emission in LAEs diffuses out through resonant scattering, or through holes in the ISM. However, most high-redshift LAEs have been discovered via ground-based narrowband imaging, which even in the best seeing conditions cannot resolve the extremely small physical sizes of LAEs of 1–2 kpc (Bond et al. 2009; Malhotra et al. 2011). Here, we report on the results of a new *Hubble Space Telescope* (*HST*) imaging survey designed to search for resolved Lyα emission from LAEs at $z \sim 4.4$ using the F658N narrowband filter on the Advanced Camera for Surveys (ACS). Throughout we use the AB magnitude system, where $m_{\rm AB} = -2.5 \log(f_\nu) - 48.6$ mag. Where applicable, we assume a concordance cosmology, with $H_{\rm o}$= 70 km s^{-1} Mpc^{-1}, $\Omega_m = 0.3$, and $\Omega_\Lambda = 0.7$. At $z = 4.4$, this corresponds to an angular scale of 6.671 kpc arcsec^{-1}.

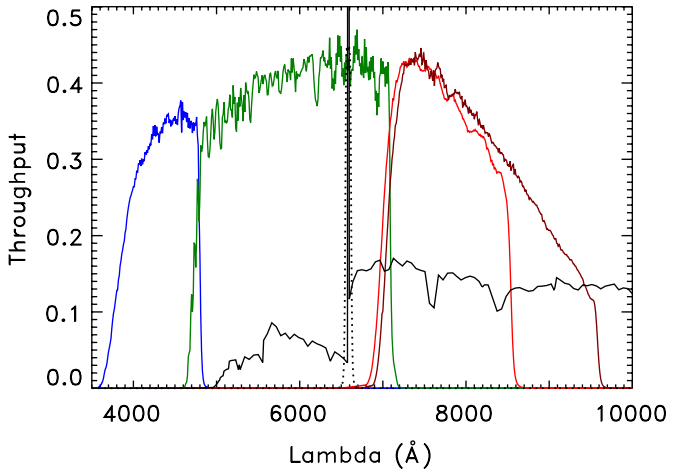

Figure 1. Model spectrum of a $z = 4.42$ LAE, showing the *HST* ACS F435W, F606W, F775W, and F814W bandpasses in blue, green, red, and brown, as well as the F658N bandpass (dotted line). From $z = 4.38$–4.45, Lyα passes through the F658N bandpass, allowing imaging of Lyα light at high redshift.
(A color version of this figure is available in the online journal.)

2. DATA

2.1. Observations

Thanks to the successful repair of ACS during Servicing Mission 4 (SM4) to *HST*, we were able to obtain ACS parallel imaging during the Early Release Science (ERS; Windhorst et al. 2011) Wide Field Camera 3 (WFC3) observations of the Great Observatories Origins Deep Survey (GOODS) Chandra Deep Field-South (CDF-S). We obtained 11 orbits per pointing over eight independent pointings. Due to the location of the WFC3 fields, all of the ACS pointings overlapped the GOODS CDF-S field, which has existing deep public data in the F435W, F606W, F775W, and F850LP ACS filters (as well as a wealth of other multiwavelength data). A detailed summary of the primary WFC3 ERS images, as well as their layout and analysis is given by Windhorst et al. (2011).

We split each parallel pointing into nine orbits with the F658N narrowband filter and two orbits with the F814W broadband filter. With a central wavelength of 6584 Å and a full width at half-maximum (FWHM) of 73 Å, the F658N observations will detect Lyα (which has $\lambda_{\rm rest} = 1215.67$ Å) from redshifts $4.386 \leqslant z \leqslant 4.445$. A model spectrum of an LAE at $z = 4.42$ is shown in Figure 1. At $z = 4.4$, the existing GOODS ACS data cover rest-frame wavelengths of ∼800 Å (F435W), 1100 Å (F606W), 1400 Å (F775W), and 1600 Å (F850LP). The F814W data will cover the continuum at ∼1500 Å, providing an independent observation in addition to the existing GOODS data set.

2.2. Data Reduction

The raw ACS data were downloaded from the Space Telescope Science Institute (STScI) archive. The ACS data were taken in 31 separate visits, with typical dithers within each visit of $< 20''$. Images from visits with central pointings separated by less than $25''$ were reduced together, yielding 17 separate reductions. The raw images were processed using the `calacs` task,

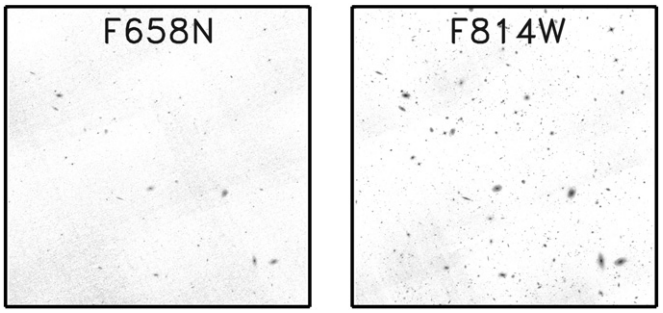

Figure 2. F658N (left) and F814W (right) image of GOODS-S section 23. This was the only GOODS-S section which was completely covered by our observations. The narrow bandpass of F658N is apparent when comparing the depths of these images, as many fewer objects are apparent in F658N even though the exposure times were longer.

which is in the stsdas package in IRAF.[21] This task provides routine calibration, including bias, dark, and flat-field corrections, using the most recent ACS reference files taken after SM4 retrieved from the *HST* archive. ACS data obtained after SM4 suffer a low-level striping pattern. We implemented a custom-built script (provided by N.A.G.) to remove this pattern prior to the flat-field correction.

The calibrated and pattern-corrected images were cleaned of cosmic rays, distortion-corrected, registered, and combined using the task `multidrizzle` (Koekemoer et al. 2002). Upon completion of the initial run of `multidrizzle` in each visit, it was apparent that the registration was not ideal, as stars in the combined images appeared elongated. We thus ran custom-built scripts (provided by A.M.K.) on a visit-by-visit basis to correct the World Coordinate System (WCS) in the headers of the individual frames, solving for the relative astrometric shifts between frames (Windhorst et al. 2011). `Multidrizzle` was then run a second time to create a final, combined image for each visit. As we planned to use the existing GOODS ACS data in our analysis, we used the GOODS ACS image sections as reference images when running `multidrizzle`. In order to correct for small astrometric differences between the GOODS data and these new ACS data, we first ran `multidrizzle` with no reference image, and performed photometry using the Source Extractor software package (hereafter SExtractor; Bertin & Arnouts 1996) to identify objects in the image. We did the same to the relevant GOODS section, and then ran the IRAF tasks `xyxymatch` and `geomap` to match common objects between the two frames, and construct a shift file. This shift file was used for the final iteration of `multidrizzle` to create F658N and F814W images matched to each GOODS section covered by our observations. Our final data set was composed of one image in each of the two filters for the 11 GOODS-S sections that we covered: 12, 13, 14, 22, 23, 24, 32, 33, 34, 42, and 43. Typical exposure times in the reduced data sets are 11,000 s in F658N and 2200–2500 s in F814W. Images of section 23 in the F658N and F814W bands are shown in Figure 2.

2.3. Catalog Construction

We created narrowband-selected catalogs for each observed GOODS-S section using SExtractor in two image mode, with the F658N image for each section as the detection image,

[21] IRAF is distributed by the National Optical Astronomy Observatory (NOAO), which is operated by the Association of Universities for Research in Astronomy, Inc. (AURA) under cooperative agreement with the National Science Foundation.

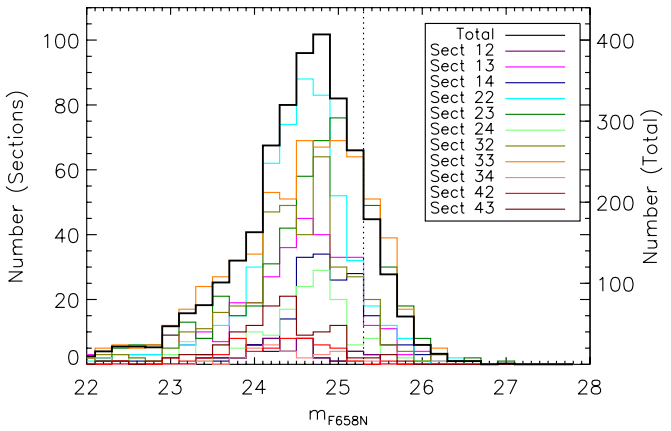

Figure 3. Number counts of objects in the F658N data. The colored histograms denote the numbers in each section, with the values being given by the left-hand vertical axis. This thick black line denotes the total combined number counts, with the values being given by the right-hand vertical axis. The varying number of objects per section is related to the amount of section area which received F658N coverage. The dotted line denotes where the total number counts fall to 50% of their peak value, which is at $m_{F658N} = 25.3$.

(A color version of this figure is available in the online journal.)

and our F658N and F814W images, as well as the GOODS F435W, F606W, F775W, and F850LP images as the measurement images. We used identical SExtractor parameters as used in GOODS. The final catalog encompassing all covered sections includes 3081 narrowband-selected objects, with fluxes measured in 0.″7 diameter apertures, as well as estimates of the total flux using SExtractor's MAG_AUTO measurement.

Initial flux errors were taken to be the calculated SExtractor errors. We checked these errors by measuring our own errors in each image. This was done by measuring the flux in 10^4 randomly placed 0.″7 diameter apertures in each of the six images, and then examining the spread of these fluxes (this was done in GOODS-S Section 23, as this was the only section which had complete coverage by our F658N and F814W data due to the unfavorable positioning of the parallel exposures with respect to the GOODS sections). The characteristic 1σ error for each image was taken as the σ of a Gaussian fit to a histogram of the flux distribution. Comparing this error to the median SExtractor error in each image, we find that SExtractor underestimated the errors by up to $\sim$20% (with the exception of the F814W data, where SExtractor overestimated the errors by 18%). While we trust our independently computed errors as being indicative of the global uncertainty in the image, the errors computed by SExtractor include information on the local background. We thus scaled the median SExtractor error to match the global uncertainty in each band. The derived 5σ limits for each band in a 0.″7 diameter aperture are 25.0 (F658N), 27.1 (F814W), 27.4 (F435W), 27.6 (F606W), 27.0 (F775W), and 26.8 (F850LP). Number counts of objects in the F658N images are shown in Figure 3, showing a peak at $m_{F658N} \sim 24.8$ mag.

3. SAMPLE SELECTION

3.1. Spectroscopically Confirmed LAEs

In Finkelstein et al. (2008) and Finkelstein et al. (2009b), a sample of 14 LAEs were discovered in the GOODS-S field using ground-based narrowband selection. These studies used three overlapping narrowband filters, centered at 6560 Å (hereafter NB656), 6650 Å (NB665), and 6730 Å (NB673) to discover LAEs at $z \approx 4.4$–4.5. Samples of 4, 2, and 8 candidate LAEs

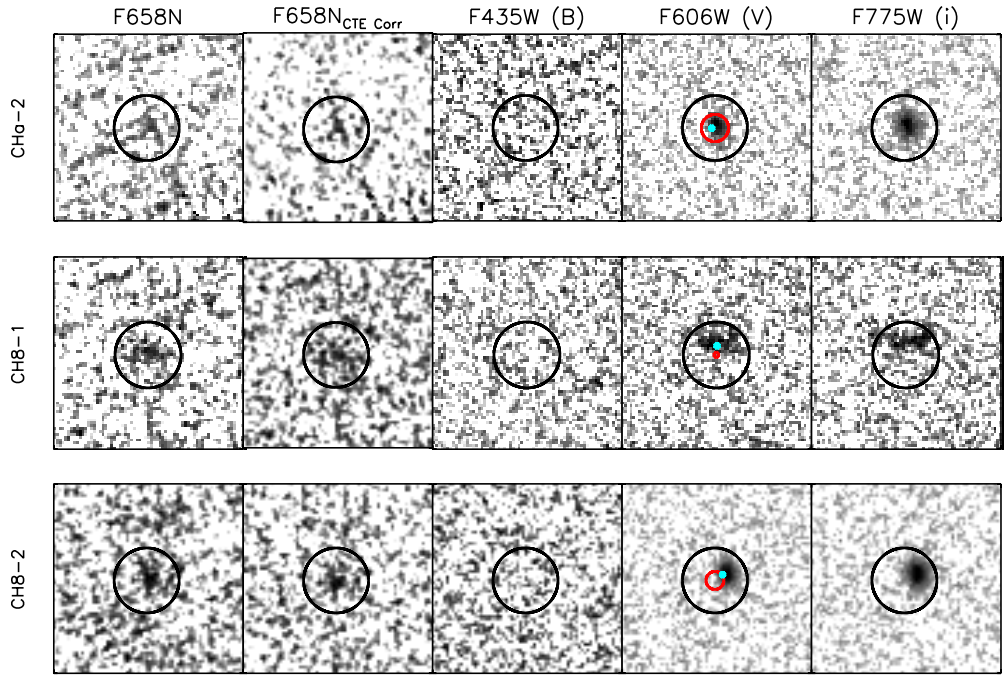

Figure 4. Cutouts of the three LAEs in our sample, 2″ on each side. The black circles are centered on the F658N centroid, with a 0.″7 diameter. The F658N data are from our program, while the remaining images are from the GOODS data set. Object CHa-2 is near an image edge, thus the lower right corner of this stamp is not real data. Although trailing due to charge-transfer inefficiency is apparent in object CHa-2 (as blurring from lower left to upper right), the narrowband flux is still detected at 3.9σ in a 0.″7 diameter aperture. The second column shows the CTE-corrected stamps, as discussed in Section 5.2.4. The CTE correction needs to be verified with newer calibration data before it can be folded into the analysis, but improvement in the background can be seen, especially near LAE CHa-2. The F435W data probe rest-frame $\lambda \sim 800$ Å at z =4.4, thus the non-detections in this image are expected. The cyan circle in the F606W images denotes the Lyα emission centroid after correction for a systematic positional offset between the WCS of the new F658N data and the existing GOODS data. The red circle denotes the 1σ uncertainty on the positional offset. These uncertainties are large in CHa-2 and CH8-2. However, the offset can be computed to a high precision in CH8-1, and we find that the apparent offset between the Lyα and UV emission can be explained by WCS differences in the two data sets.

(A color version of this figure is available in the online journal.)

were discovered in the three images, with 5σ depths of 24.9, 25.0, and 25.2 mag, respectively.[22] The ACS F658N filter can measure Lyα emission from galaxies at z = 4.38–4.45; thus, it would also observe Lyα from objects discovered in the red half of the NB656 filter, or in the blue half of the NB665 filter. Of the six candidate LAEs discovered in these two filters, three fall in the area covered by our F658N observations. These three objects are CHa-2, CH8-1, and CH8-2, using the nomenclature from Finkelstein et al. (2009b; where CHa denotes CDFS Hα, i.e., NB656, and CH8 denotes CDFS Hα + 80 Å, i.e., NB665). Images of these three objects are shown in Figure 4. These objects have rest-frame Lyα EWs of 167, 176, and 53 Å, respectively, as measured by ground-based photometry in Finkelstein et al. (2009b).

Although these objects were previously selected via narrowband observations from the ground, they had yet to be spectroscopically confirmed. We recently obtained optical spectroscopy of these three objects with the Inamori Magellan Areal Camera and Spectrograph (IMACS) at the Magellan Baade Telescope on 2009 November 11 and 12 (NOAO PID 2009B-0371, PI: Finkelstein). The full details of this spectroscopic data set will be presented in a future paper (Z. Zheng et al. 2011, in preparation), but in brief, each object was observed as part of a 4 hr slit-mask integration, with the $f/2$ camera and the 300 lines mm^{-1} grating blazed at 17.°5 (giving $R \simeq 1000$). The reduced, one-dimensional spectra of these three objects are shown in Figure 5. Each object exhibits a single emission line with no significant continuum light, indicative of Lyα emission at high redshift. Fitting a Gaussian curve to these emission lines, we find redshifts of CHa-2, CH8-1, and CH8-2 of 4.414, 4.434, and

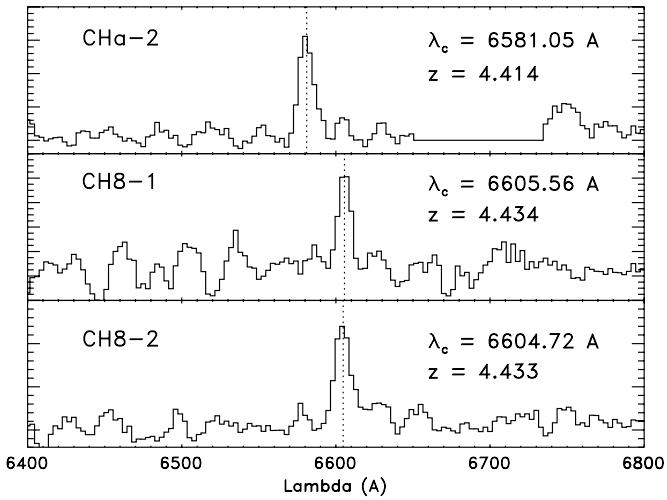

Figure 5. Magellan/IMACS optical spectra of the three LAEs in our data, centered around the observed Lyα emission line. The vertical scale is in arbitrary flux units. From the position of the emission line, and the lack of any other emission lines in the full spectra, we confirm that all three objects are LAEs at $z \approx 4.4$. This confirms that the emission line flux we detect in the F658N image is Lyα emission from these objects.

[22] The image depths in the NB665 and NB673 images were computed in 2.″3 diameter apertures. The depth in the NB656 image is based on point-spread-function fitting, as described in Finkelstein et al. (2008).

Table 1
Properties of the LAEs

Object	$z_{Ly\alpha}$	R.A. (J2000)	Decl. (J2000)	m_{F658N} (mag)	m_{F606W} (mag)	m_{F775W} (mag)	$r_{h,F658N}^{APER}$ ($''$)	$r_{h,F658N}^{APER}$ (kpc)	$r_{h,F775W}^{APER}$ ($''$)	$r_{h,F775W}^{APER}$ (kpc)
CHa-2	4.414	03:32:39.77	−27:51:14.97	24.9 ± 0.3	26.57 ± 0.09	25.56 ± 0.06	$0.11^{+0.35}_{-0.04}$	$0.73^{+2.33}_{-0.27}$	$0.10^{+0.01}_{-0.01}$	$0.67^{+0.07}_{-0.07}$
CH8-1	4.434	03:32:49.01	−27:49:02.08	25.2 ± 0.2	27.06 ± 0.14	26.54 ± 0.14	$0.21^{+0.16}_{-0.08}$	$1.40^{+1.07}_{-0.53}$	$0.16^{+0.03}_{-0.03}$	$1.07^{+0.27}_{-0.20}$
CH8-2	4.433	03:32:54.04	−27:50:00.83	24.6 ± 0.2	25.93 ± 0.05	24.98 ± 0.04	$0.20^{+0.13}_{-0.07}$	$1.33^{+0.87}_{-0.47}$	$0.10^{+0.00}_{-0.01}$	$0.67^{+0.07}_{-0.00}$

Notes. The position is the centroid of the F658N counterpart. All magnitudes were measured with $0\farcs70$ diameter apertures. Half-light radii (r_h) were converted from arcsec to kpc assuming all objects are at $z = 4.4$, which gives an angular scale of 6.671 kpc arcsec^{-1} for our assumed cosmology.

4.433, respectively, placing the Lyα emission line of each object in the bandpass of the ACS F658N filter.

Examining these objects in Figure 4, they all appear robustly detected in the F658N image. However, especially in the case of CHa-2, the noise due to poor charge-transfer efficiency (CTE) in the nearly decade-old CCDs onboard ACS is apparent. Nonetheless, when we consult our narrowband-selected catalog, we find that CHa-2, CH8-1, and CH8-2 are all formally detected, with detection significances of 3.9σ, 5.0σ, and 5.4σ, respectively. Combined with the fact that LAEs were previously known to reside at these locations, we are confident that we are in fact detecting Lyα emission with ACS. Details on these three LAEs are provided in Table 1.

3.2. Photometric Redshift Selection

In addition to objects previously selected on the basis of their Lyα emission at $z \approx 4.4$, we have also examined the F658N images for objects which are likely to reside at $z \sim 4.4$ based on their spectral energy distribution. We selected objects at this redshift from two catalogs, both from S. Cohen et al. (2011, in preparation). The first consists of ∼15,000 objects with spectrophotometric redshifts computed using both ACS broadband and grism slitless spectroscopic data from the Probing Evolution and Reionization Spectroscopically (PEARS) program (PI: S. Malhotra). The second catalog consists of ∼8000 photometric redshifts measured over the entire GOODS-S region, using VLT/VIMOS U (Nonino et al. 2009), GOODS/ACS v2.0 B, V, i', z', and GOODS VLT/ISAAC v2.0 J-, H-, and K-band data (Retzlaff et al. 2010).

We examined these objects for galaxies with best-fit (spectro)photometric redshifts of $4.38 \leqslant z \leqslant 4.45$, placing any Ly$\alpha$ emission in the F658N bandpass. We also included objects that had this redshift slice contained within the 68% confidence range on their spectrophotometric redshift. We found 106 objects meeting these criteria. We then matched these objects to our F658N catalog, using a matching radius of $0\farcs5$, and we found six objects that have F658N counterparts. The low number of matched objects is expected, as only galaxies exhibiting Lyα emission at the specific redshift placing it in the F658N bandpass would be detected in the narrowband data. These objects were visually inspected in the F658N data. Of these six objects, only two have moderate narrowband excesses (m_{F606W}–m_{F658N} = 0.6 and 1.8 mag). However, both objects have significant detections in the F435W band. This band is entirely blueward of both the Lyα and Lyman continuum breaks at $z \approx 4.4$ (see Figure 1); thus, there should not be an F435W detection if these objects were truly at $z \approx 4.4$. We conclude that these two objects are low-redshift interlopers, and we exclude them from further study.

4. RESULTS

With our sample of three F658N-detected $z = 4.4$ spectroscopically confirmed LAEs, we investigate their light profiles, as well as the location of their Lyα emission.

4.1. Positional Differences between Lyα and Rest-frame UV Emission

In a number of objects the Lyα emission appears offset from the centroid of the rest-frame UV emission. If this effect is real, it is quite interesting, as it could indicate that Lyα is escaping only after scattering off gas or dust outside the primary stellar population, perhaps due to outflows in the ISM (e.g., Windhorst et al. 1998; Waddington et al. 1999). However, we first need to investigate if the offset is real, or if it is an artifact of mismatches between the WCS of the new F658N data and the existing GOODS-S data.

We investigated these offsets by examining the relative pixel positions of all objects in the images around the LAEs. To find these objects, we first ran SExtractor on both the F658N and F606W images, using each image as its own detection image, such that we obtained object coordinates native to each image. On an LAE by LAE basis, we first searched the F658N catalog for all objects in a given section, excluding objects near the edge of our images, as well as objects below the point where the number counts fall to 50% of their peak value, which is at 25.3 mag. We then computed the distance in pixels from the LAE to each of these objects. We selected objects within a threshold radius, which ranged from 500 to 3000 pixels in 100 pixel increments, and matched them to objects in the F606W catalog, keeping objects that were matched within 20 pixels (which is larger than the largest apparent shift; see Figure 4). By including only objects near the LAE, we ensure that we are locally measuring any offset between the F658N and F606W image frames. At a 1000 pixel radius, on average a dozen matches were found, increasing to ∼40 matches by 2000 pixels. The pixel offsets were then computed as the mean difference between the narrowband position and the broadband position for each of the matched objects. An estimate of the uncertainty on these shifts was taken to be the standard deviation of the positional differences for the matched objects.

Figure 6 shows an example of this process, showing the results for LAE CH8-1. We plot lines showing both the pixel offsets, as well as the offset uncertainties as a function of search radius. We chose offset values for each object to be the pixel offset value at the radius where the offset uncertainty was a minimum. For this object, the x-offset is negligible (0.24 ± 0.98 pixels), while the y-offset is significant, at 3.25 ± 0.73 pixels. Investigating Figure 4, this offset would move the broadband counterpart down vertically, bringing it more in line with the narrowband position. This is shown by the cyan circle in Figure 4. A similar

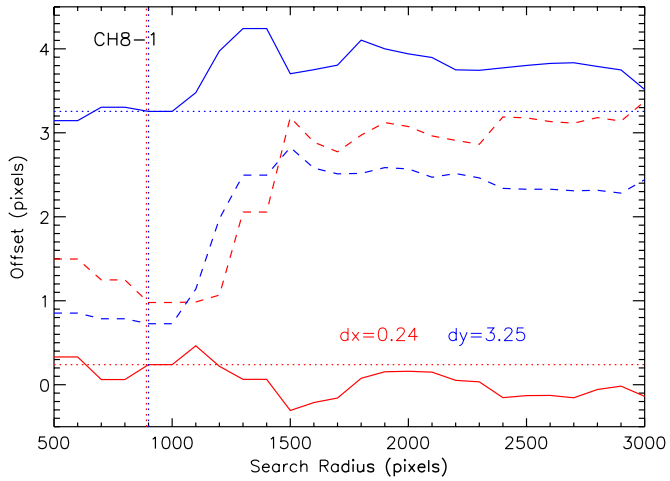

Figure 6. Derived pixel offsets between the F658N and the GOODS F606W data for objects near LAE CH8-1, vs. the search radius used to find objects to derive the offset. Red and blue denote the *x*- and *y*-offsets, respectively, while the solid and dashed lines denote the offset and offset uncertainty. Offsets were derived using objects within 500–3000 pixels, in 100 pixel increments. The value of the offset was defined to be the offset derived from the search radius which produced the smallest offset uncertainty (designated by the dotted lines). In this object, the offset uncertainties for both *x* and *y* reached a minimum at 900 pixels, thus the pixel offsets were taken to be the values at that search radius. At larger search radii, the offset uncertainties increase dramatically.

(A color version of this figure is available in the online journal.)

process was done for the remaining objects, and these offsets are tabulated in Table 2.

In Figure 4, we show the corrected Lyα emission position by a small cyan circle, and the typical offset error as a red circle (where the radius of the circle is the mean of the *x*- and *y*-offset errors for a given object). We find that in CHa-2 and CH8-2, the uncertainties on the derived pixel offsets are large, and thus any apparent offset would be at low significance. However, in CH8-1, the offset uncertainties are small, and we can see that the computed offset is consistent with the centroid of the UV emission. Thus, while the Lyα and UV emission in CH8-1 appear to be offset, this can be explained by relative offsets between the two data sets.

We conclude that while it is possible that ISM scattering effects can result in an offset between the apparent positions of Lyα and rest-frame UV emission, we cannot conclusively support this with our data. The most convincing offset is in CH8-1, as the offset is large. However, this is also the only object where the offset uncertainties are small enough that we can reasonably correct the Lyα emission position, and we find that its corrected position is then coincident with the UV emission. In addition, when inspecting the F814W data taken at the same time as the F658N data, the apparent offset between F658N and F814W is much less. We move forward assuming that the Lyα emission is coincident with the rest-frame UV emission in all objects.

4.2. Physical Size of Lyα Emission

4.2.1. Individual Objects

In order to measure the physical sizes of the LAEs in our sample in both their Lyα and rest-frame UV continuum light, we employed the method of Bond et al. (2009). We first cut out 101 × 101 pixel (3″ × 3″) postage stamp FITS images centered on each LAE in both the F658N and F775W data (we used the F775W rather than the F606W data for the rest-frame UV as it is completely redward of Lyα at this redshift). We then ran SExtractor on each stamp, using the stamp as both the detection and measurement image to determine the flux-weighted center of the object, as well as to determine whether an object is made up of sub-clumps that might have been split up by SExtractor. Experimenting with various values of the DEBLEND_NTHRESH parameter, we found that none of our LAEs can be split into multiple objects; thus, we conclude that all objects in our sample are composed of single dominant components. Inspecting the SExtractor results, we find that (as expected) each object is detected in both F658N and F775W.

Using the SExtractor-derived center in the F658N and F775W images, respectively, we measured the flux in a series of 32 apertures, with radii ranging from 0.″015 to 1.″2 using SExtractor. In order to ensure that the CTE-affected background was subtracted as well as possible, we manually subtracted the background prior to running SExtractor, using the iterative mean computed with the IDL task djs_iterstat.pro.[23] We then forced SExtractor to assume a background value of zero. Previously measured half-light diameters of LAEs are ∼0.″2–0.″4 (Bond et al. 2009, 2010), thus we assume that the flux at a radius of 0.″6 approximates the total flux. We then compute the radius at which the flux is half of the flux at $r = 0.''6$, and use that as an estimate of the half-light radius (r_h).

Values of r_h were computed for each object in F658N and in F775W, and are tabulated in Table 1. The curves of growth (CoGs) of each object in both bands are shown in Figure 7. We also show the uncertainty in the CoGs as the shaded region. We used a similar exercise as explained in Section 2.3 to compute the flux uncertainty in all 32 apertures. We ran simulations on each image section which contained one of our LAEs for each aperture size used. For each simulation (i.e., for each different combination of aperture and image section), we placed apertures at 10^4 random positions, such that the fluxes in concentric apertures were not measured at the same position. This ensures that our aperture flux errors are not correlated. The flux uncertainty in each aperture is computed as the standard deviation of the 10^4 flux values in each aperture. We then used these errors to compute uncertainties on our derived half-light radii by running a separate series of 10^4 Monte Carlo simulations.

In each simulation, we vary the flux at each point in the CoG by a random number (drawn from a Gaussian distribution centered at zero with $\sigma = 1$) multiplied by the flux uncertainty, and rederive the half-light radius. However, we found that

Table 2
Corrections to Narrowband Emission Position

Object	Δx (pixels)	Δy (pixels)
CHa-2	-1.17 ± 5.10	-0.08 ± 4.66
CH8-1	0.24 ± 0.98	3.25 ± 0.73
CH8-2	2.74 ± 4.16	2.09 ± 2.28

Notes. The derived pixel corrections to the F658N emission position due to WCS differences between the F658N and the GOODS data. The corrected narrowband emission position is given by the cyan circles in Figure 4, while the positional uncertainties are shown by the red circles.

[23] From the IDLUTILS package: http://spectro.princeton.edu/idlutils_doc.html/.

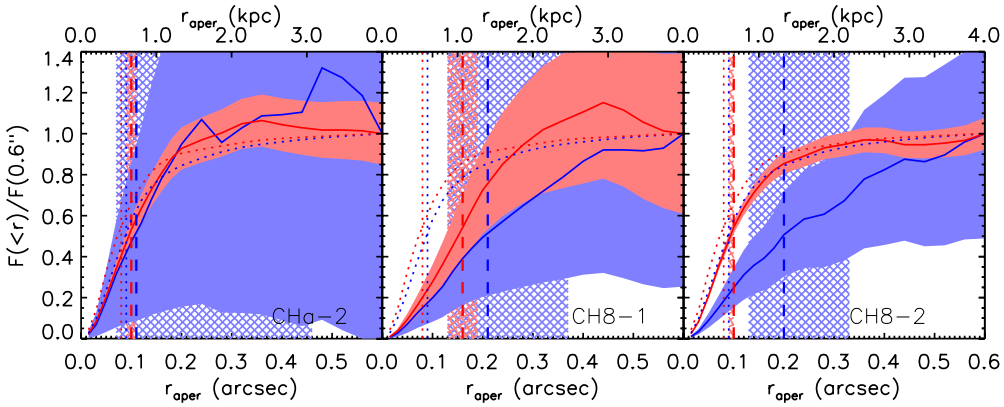

Figure 7. Measured curves of growth from aperture photometry for the objects in our sample in blue and red for F658N and F775W, respectively. The shaded regions show the 1σ uncertainties on the CoGs. The colored dashed lines denote the half-light radii, with the cross-hatched regions denoting the 1σ uncertainties on the radii. The colored dotted lines denote the resolution limit of the given image derived from the sizes of stars in the images, while the dotted curves show the CoGs of the image PSFs. The CoG of Lyα appears significantly more extended than that of the rest-frame UV continuum in CH8-2, resulting in larger Lyα half-light radii. Note that although it cannot be seen in the figure, the blue shaded region for CH8-1 extends through much of the extend of the red shaded region.

(A color version of this figure is available in the online journal.)

varying the fluxes in all apertures created very uneven COGs, making estimates of the half-light radius difficult. We opted to thus only vary the flux in the largest aperture, as the derived spread of half-light radii was similar to that when varying all aperture fluxes, and the simulated COGs were smoother (allowing more accurate determination of the half-light radius in each simulation). We used the simulation results to compute the 68% confidence region on the half-light radius for each band for each object. These confidence regions on the half-light radii are shown as cross-hatched regions in Figure 7. Typical uncertainties on r_h are $\sigma_{r_h} \sim 0\farcs10$ in F658N and $\sim 0\farcs01$ in F775W.

To determine whether a particular object is resolved, we performed the above analysis on a point-spread function (PSF) made from stars in both the F658N and F775W data. These PSFs were made by adding together images of five stars identified in section 23. We first cut out 101 × 101 pixel postage stamps around each star. In order to be sure the stars were centered, we computed the difference between the centroid of the star and the center of the array. If the difference was more than 0.2 pixels in either direction, we subsampled the image by a factor of 10, and shifted the star by 1 pixel for each tenth of a pixel it was offset from the center (the subsampling was done using the IDL function `frebin`, which uses bilinear interpolation). The image was then binned back down to the native resolution. This process was run iteratively on each star until they were all <0.2 pixels from the array center. Each star was normalized to its peak flux. The PSF was then calculated as the median of the five stars at each pixel position, and then normalized to a total flux of 1. Measuring the half-light radii of the PSF in each band in the same manner as above, we measure an image resolution of $r_h = 0\farcs09$ in F658N, and $r_h = 0\farcs08$ in F775W. Objects with r_h at or less than these values are considered unresolved at the limit of *HST*+ ACS in their respective bands.

For our sample of LAEs, we found half-light radii in the F658N image of $0.11^{+0.35}_{-0.04}$, $0.21^{+0.16}_{-0.08}$, and $0.20^{+0.13}_{-0.07}$ arcsec for CHa-2, CH8-1, and CH8-2, respectively. In the F775W image, we found LAE half-light radii of $0.10^{+0.01}_{-0.01}$, $0.16^{+0.03}_{-0.03}$, and $0.10^{+0.00}_{-0.01}$ arcsec for CHa-2, CH8-1, and CH8-2, respectively. Comparing these sizes to the PSFs discussed above, we find that we can definitively resolve 2/3 LAEs in the F658N image, and 1/3 LAEs in the F775W image. At $z = 4.4$, the angular scale is ~6.671 kpc arcsec^{-1} (for our assumed cosmology); thus, these sizes correspond to 0.7–1.4 kpc in Lyα, and 0.7–1.1 kpc in the rest-frame UV continuum.[24]

4.2.2. Stacking Analysis

As shown in Table 1, the signal to noise of the individual detections in the F658N image are not large. Thus, in order to obtain a more robust estimate of the *average* half-light radii of LAEs, we have performed a stacking analysis. Hathi et al. (2008a) show in detail how such image stacking is justified for similar galaxies at similar redshifts, using the HUDF *B*, *V*, and *i*′ dropouts at $z = 4$, 5, and 6, respectively.

Using the cutout stamps described in the above section, we first centered each LAE on the central pixel of each stamp using the iterative technique described above for the PSF, requiring the SExtractor-derived center to be within 0.2 pixels of the center of the stamp. This step was performed separately for each object for each band, such that the F658N stamps were centered on the F658N emission, and the F775W stamps were centered on the F775W emission. Each centered LAE stamp was then normalized to its peak flux. A stacked image was then created in each band by taking the median of each pixel value from all three LAEs. Figure 8 shows the stacks of the three LAEs in both bands, with the contours denoting levels of constant brightness, as well as three-dimensional surface-brightness profiles.

We measured half-light radii of each of the two stacks (one for each band) in the same manner as the above section. The results from this analysis are shown in Figure 9. These stacking results confirm our observations of the individual objects, in that the Lyα emission is more extended than the rest-frame UV continuum emission, with $r_h = 0.16^{+0.02}_{-0.01}$ arcsec in F658N, and $r_h = 0.10^{+0.01}_{-0.00}$ arcsec in F775W. These angular sizes correspond to physical half-light radii of 1.07 ± 0.08 and 0.67 ± 0.05 kpc for the F658N and F775W emission, respectively.

[24] The Year 7 *Wilkinson Microwave Anisotropy Probe* cosmology (H_o = 70 km s^{-1} Mpc^{-1}, $\Omega_m = 0.27$, and $\Omega_\Lambda = 0.73$; Komatsu et al. 2011) gives an angular scale of 6.899 kpc arcsec^{-1}, which would give physical sizes 4.3% larger than our assumed cosomology.

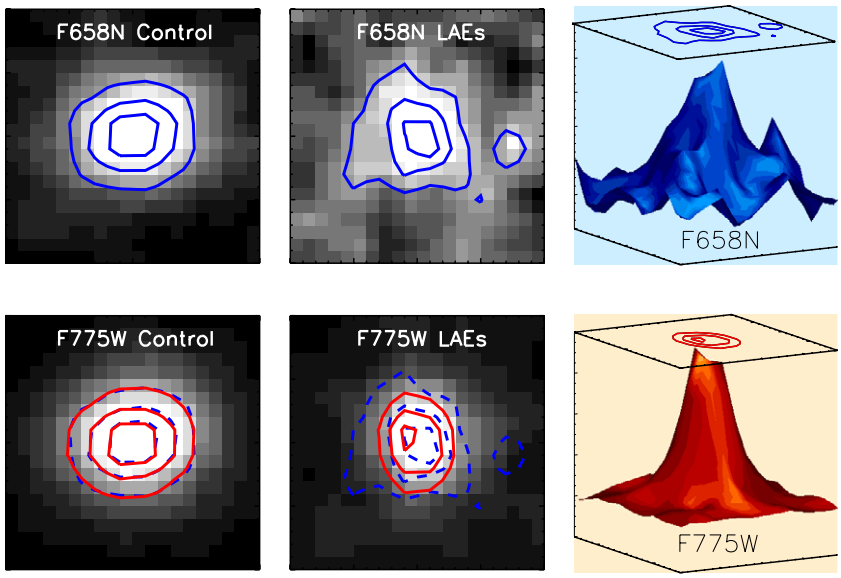

Figure 8. Left: stacked images of the 28 control-sample galaxies (galaxies with $m_{F658N} \sim 25$ with no narrowband excess) in the F658N band (top) and the F775W band (bottom), with both images normalized to their peak flux. Middle: stacked images of the three LAEs. The light in the F658N image is primarily due to Lyα emission in these galaxies, while the F775W band shows the rest-frame UV continuum emission longward of Lyα. The LAEs appear larger in F658N than in F775W, implying that the Lyα emission in these galaxies is more extended than the rest-frame UV continuum emission. The control-sample galaxies appear the same size in both the F658N and F775W images, implying that the extended F658N size of the LAEs is not due to image noise. The contours represent regions of constant flux, corresponding to 0.3, 0.5, 0.7, and 0.9 of the peak flux. The F658N contours are also shown in the F775W image as dashed curves. Right: three-dimensional surface profile of the LAE F658N stack (top) and the F775W stack (bottom). The contours are the same as in the middle panels. The F775W stack has a steeper profile (and thus a smaller half-light radius), as shown by the more compact surface profile, and the denser contours.

(A color version of this figure is available in the online journal.)

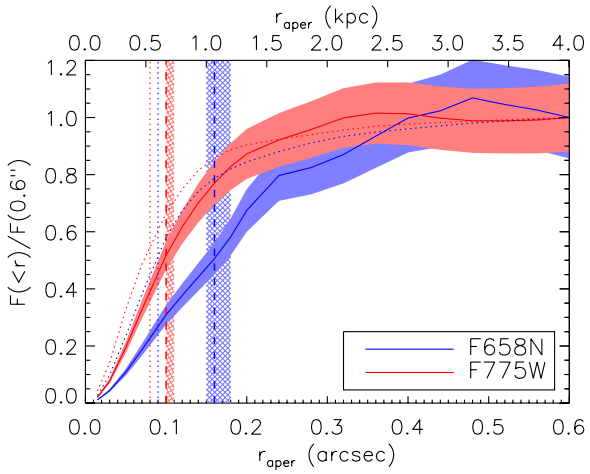

Figure 9. Measured light profiles from aperture photometry for the stack of our sample of three spectroscopically confirmed LAEs in blue and red for F658N and F775W, respectively. The lines, shaded and cross-hatched regions are the same as in Figure 7. Both stacks exhibit the same result as the individual objects—Lyα emission appears more extended than the rest-frame UV continuum.

(A color version of this figure is available in the online journal.)

5. DISCUSSION

5.1. Rest-frame UV Emission

Inspecting Figure 7, one can see that all three LAEs are compact in their rest-frame UV continuum with half-light radii of $r_h < 1.1$ kpc. This is consistent with previous studies of high-redshift galaxies. Ferguson et al. (2004) studied the rest-frame UV sizes of Lyman-break-selected galaxies at $z > 3$, and photometric-redshift-selected galaxies at $1 < z < 3$ using data from *HST*. They found half-light radii from 0.″25 to 0.″4 at $z > 2$ (∼2–3 kpc), rising to $r_h \sim 0.''65$ at $z \sim 1$ (∼5 kpc) for galaxies with $0.7\ L^* < L_{UV} < 5\ L^*$. Similar size evolution has been found to extend out to $z \sim 6$ (Hathi et al. 2008b) and $z = 7$–8 (Oesch et al. 2010), where $L_{UV} \sim L^*$ LBGs have $r_h \sim 1$ kpc.

Relatively few LAEs have had their morphologies studied. Recently, Bond et al. (2009) studied the rest-frame UV morphologies of a sample of LAEs at $z \sim 3.1$ from the MUSYC survey (Gawiser et al. 2006). They found that LAEs are typically at least as compact as LBGs, with $r_h \lesssim 2$ kpc, and that the Lyα emission is likely coincident with the UV emission (within <1 kpc). Gronwall et al. (2010) studied the same sample, examining the better detected LAEs (signal-to-noise ratio (S/N) > 30) in greater detail, finding that their rest-frame UV light is very concentrated, and that they have Sersic indices indicative of disk-like morphologies in most instances ($0 < n < 2$).

5.2. Lyα Emission

5.2.1. Previous Results

Prior to this study, only two high-redshift Lyα-selected galaxies have been detected in their Lyα light at *HST* resolution (i.e., using space-based narrowband data), published recently by Bond et al. (2010). In this study, Bond et al. (2010) obtained *HST*/WFPC2 F502N imaging of $z \sim 3.1$ LAEs, obtaining detections of two out of the eight LAEs they targeted. They concluded that these objects have Lyα half-light radii < 1.5 kpc, similar to their rest-frame UV sizes, with the Lyα emission coincident within 0.5 kpc of the rest-frame UV emission. Rhoads et al. (2009) also examined the relative sizes of LAEs in Lyα and the UV continuum using ACS grism spectroscopic data from the PEARS survey by examining the sizes of the objects in the spatial dimension. They did not find evidence of an extended Lyα halo in a stack of the spectra from all 39 $z \sim 5$ galaxies in their sample. However, when stacking only the 10 galaxies with

Lyα observed in emission, they found that the spatial width of the spectrum at the position of Lyα had FWHM = 0.″26, while the same measurement on the adjacent UV continuum yielded FWHM = 0.″19. Finally, Nilsson et al. (2009) found that many of their $z \sim 2.25$ LAEs were resolved from the ground in the narrow band (with FWHM $> 1''$), while these objects were consistent with being unresolved in the r' band, which they attributed as being due to diffuse scattering of Lyα. They also found that two of their 170 LAEs had FWHM $> 3''$ in the narrow band, with broadband FWHM $\sim 2''$. These few objects may be analogous to Lyα blobs, though Nilsson et al. (2009) determine that they are not large enough (15 kpc) to meet the definition of a blob. Nonetheless, recent results by Yang et al. (2010) imply that the distribution in Lyα sizes between LAEs and Lyα blobs may be continuous, and our results, along with those of Nilsson et al. (2009) are beginning to find objects along that distribution.

5.2.2. Individual Objects

Our positive detections of the three spectroscopically confirmed LAEs more than double the total number of detected high-redshift LAEs with high-resolution imaging of their Lyα light. Investigating the Lyα light profiles of our LAEs, we find that the Lyα emission appears relatively compact as well, with the half-light radius in every object at $\leqslant$1.4 kpc, and the mean size of $\sim$1.2 kpc consistent with the Lyα sizes of the two galaxies detected by Bond et al. (2010).

Comparing the CoGs of the Lyα and rest-frame UV continuum light in individual LAEs in Figure 7, we find that only CH8-2 has a Lyα half-light radius *larger* than the rest-frame UV at $>1\sigma$ significance. CHa-2 is near the limit of our resolution in both the Lyα and UV continuum light. The CoGs of CH8-1 and CH8-2 are very similar, with the rest-frame UV (F775W) profile rising quickly, reaching the "total" flux at a radius smaller than the Lyα (F658N) CoG, which is rising more slowly. Examining the uncertainties on the CoGs, the difference between the Lyα and rest-frame UV is at a $>1\sigma$ significance for much of the profile for CH8-2, while it is $<1\sigma$ for CH8-1, thus the difference in half-light radius for CH8-1 is not significant.

Investigating Figure 7, it is apparent that the low significance of the CHa-2 detection is hindering our measurement of its CoG, and thus its half-light radius measurement. Additionally, for the remaining two objects, while their CoGs indicate larger half-light radii in Lyα than in the rest-frame UV continuum, one will notice that their F658N CoGs continue to increase out to the maximum radius. This effect is due to the CTE contribution to the background, which is a primarily positive signal caused by the overlapping CTE tails from the plentiful cosmic rays. It is thus possible that this CTE effect is artificially increasing the radii we measure in the F658N data.

It is thus prudent to examine these data to ensure that the result of larger sizes in the F658N data is a physical effect, and not an artifact of the data. We have performed a check on our results by measuring the sizes of a control sample of galaxies that has F658N magnitudes similar to the LAEs in our sample, of $24.6 \leqslant m_{\rm F658N} \leqslant 25.2$, yet have no Lyα emission. For this test sample, we also required that the objects be detected at 5σ significance in both F658N and F775W, that $22 < m_{\rm F775W} < 29$, and that the difference between the F658N and F606W magnitudes be $<$0.1 mag. Out of our whole F658N-selected catalog, this yielded 67 objects. We further culled the sample by excluding objects near image edges, as well as highly extended or clumpy objects, leaving a final sample of 28 objects. We measured the sizes of these objects in a similar manner as the LAEs in our main sample. We found the median of the ratio of $r_{h,\rm F658N}/r_{h,\rm F775W}$ to be 1.15, with a standard deviation of 0.33. However, the uncertainty on the radii is much higher in the higher ratio objects; thus, we computed a mean weighed by the uncertainties on the radii, finding $r_{h,\rm F658N}/r_{h,\rm F775W} = 1.08 \pm 0.04$. This analysis shows that there is a slight systematic effect increasing the radii for objects in the F658N images over the F775W images. However, with the exception of CHa-2 (which has the least significant detection, and thus is the most difficult to make conclusions about), this $\sim$10% effect is small when compared to the ratio of the radii for our three LAEs (1.1, 1.3, and 2.0 for CHa-2, CH8-1, and CH8-2, respectively) and the stack (1.6). We use the distribution of the ratios of half-light radii to place confidence levels that the measured radii ratios from our objects and stack are inconsistent with this distribution. We find confidence levels of 32%, 71%, and 96% for CHa-2, CH8-1, and CH8-2, and 89% for the stack. This implies again that it is difficult to constrain the size of CHa-2, while the remaining objects are inconsistent with the control-sample distribution at $>$70% (or $>1\sigma$). We conclude that larger F658N sizes in our sample are likely real, but a larger sample of LAEs would increase the confidence in our result.

5.2.3. Stacking Analysis

As is shown in Figure 8, stacking the objects helps to reduce the CTE-affected background. We see the same results in the stacking analysis in Figure 9 as hinted at in the individual objects, with the CoG of the rest-frame UV exhibiting a significantly steeper profile than that of Lyα, highlighted here by the smaller uncertainties on the profile due to the greater signal to noise of the stacked images. Similar to the individual results, the Lyα half-light radius of the stack of LAEs is significantly greater than that of the rest-frame UV continuum, at $\sim 4\sigma$ significance. Also of note is that both CoGs reach a value of 1 by $\sim$0.″4, and oscillate around 1 (due to image noise) at higher radii. This implies that our derived half-light radii do not depend on our choice of a maximum radius. We verified this, as changing the maximum radius from 0.″4 to 0.″8 changed the resultant half-light radii by less than 1σ.

Figure 8 highlights this result, showing the two stacked images with contours of constant brightness at 30%, 50%, 70%, and 90% of the peak flux. In the right-hand panels, we show three-dimensional surface-brightness profiles of these images. As is evident to the eye, the contours on the Lyα image are more loosely packed, and the Lyα three-dimensional image exhibits a broader slope than that of the rest-frame UV continuum image. Though the difference is slight, primarily due to the faint nature of these objects and the difficulty of space-based narrowband observations, these results are significant. In this figure, we also show the stack of the 28 "control-sample" objects discussed in Section 5.2.2. We find that the F658N and F776W contours are nearly identical, implying that the larger F658N size we measure for the stack of LAEs is not due to properties of the image itself, and is likely a physical effect.

5.2.4. Improvements to the CTE Correction

After the completion of our analysis, we were made aware of potential future improvements to the correction of the poor CTE in the ACS data (Anderson & Bedin 2010). While our analysis shows that the charge trailing is not significantly affecting our size measurements in the F658N data (Section 5.2.2), we were able to reprocess sections 13 and 22 of our F658N data using

the updated CTE correction, in order to verify our results (see Figure 4). Briefly, the correction is based on a study of the trails behind warm pixels in dark exposures. The algorithm performs a mild deconvolution to restore the flux from the trails into the delta-function warm pixels. The correction has been demonstrated to work well on backgrounds greater than five electrons, but at the time of development, sufficient data did not exist to calibrate the correction for backgrounds below this (the F658N images discussed here have backgrounds much less than this). Nevertheless, the current algorithm has been shown to correct the majority of CTE blurring, even at essentially zero background.[25] In an aperture of radius 0.″3, the CTE-corrected data are ∼0.2 mag deeper than the uncorrected data, which pushes these *HST* narrowband data deeper than the existing ground-based data.

For our three LAEs, we found F658N sizes in the CTE-corrected data of $0.18^{+0.04}_{-0.05}$, $0.21^{+0.10}_{-0.07}$, and $0.21^{+0.10}_{-0.05}$ arcsec for CHa-2, CH8-1, and CH8-2, respectively. This implies that our size measurements for CH8-1 and CH8-2 are likely not adversely affected by the CTE problems, and also that CHa-2 may in fact be resolved, and larger in Lyα than in the rest-frame UV. Stacking these objects, we find nearly identical results to our uncorrected stack, with $r_{h,\mathrm{F658N}} = 0.17^{+0.01}_{-0.01}$ arcsec and $r_{h,\mathrm{F775W}} = 0.10^{+0.01}_{-0.00}$ arcsec.

We currently plan to reprocess all of our F658N data with the CTE correction, and do a new selection for LAEs based solely on the *HST* data to increase our sample of LAEs with resolved Lyα emission. However, the CTE-correction algorithm needs to be verified at the low sky levels present in our data, and this requires new dark frames to be obtained. This work will be presented in a future paper.

5.2.5. Interpretation of Results

Our results indicate that in our sample of LAEs, the Lyα light is emitted from a larger region than the rest-frame UV continuum light. This result is intriguing, since both types of photons likely originate in the same location—the H II regions within the galaxy—thus one may expect both sets of photons to exhibit the same light profiles. However, Lyα photons are resonantly scattered by neutral hydrogen, while the rest-frame UV continuum is not. In an ISM that is homogeneous, *if* there is no dust, this resonant scattering will result in a decoupling between the observed location of Lyα emission and the rest-frame UV continuum emission, with much of the Lyα emission eventually escaping from a random location far from its origin, appearing as an extended halo. However, in recent years, we have learned that many LAEs do in fact contain dust (e.g., Pirzkal et al. 2007; Finkelstein et al. 2008, 2009b; Pentericci et al. 2009). In a dusty homogeneous ISM, where dust is evenly mixed with neutral hydrogen, resonant scattering will result in the majority of Lyα photons being absorbed by dust; thus, a pure homogeneous ISM is unlikely, given that these galaxies exhibit Lyα in emission.

On the other hand, if the ISM is *inhomogeneous*, Lyα can still escape in a scattered halo even if dust is present (Neufeld 1991; Hansen & Oh 2006; Finkelstein et al. 2007, 2008, 2009b). In an idealized case where the ISM is purely clumpy, nearly all Lyα photons can escape as they scatter off H I at the surface of the clumps and are thus screened from the dust. Even if an ISM is only partially clumpy, this geometry still allows Lyα to escape, though predominantly in a scattered halo. Additionally, if the majority of Lyα emission escapes only after scattering of the receding edge of an outflow, the (now redshifted) Lyα photons would also be decoupled from the rest-frame UV continuum, perhaps appearing in a larger halo as well.

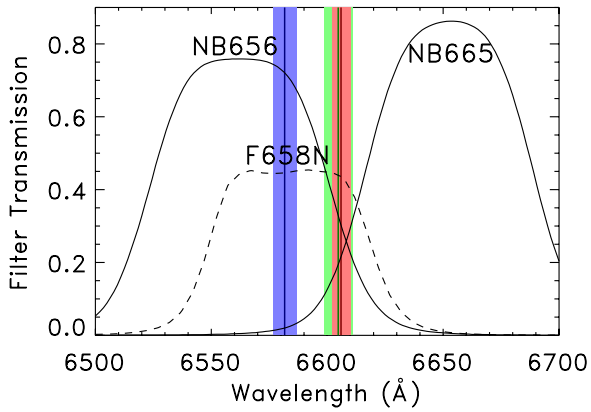

Figure 10. Filter profiles of the ground-based NB656 and NB665 filters are shown as the solid black lines, while the *HST*/ACS F658N filter profile is shown as the dashed black line. The position of the Lyα emission lines for CHa-2, CH8-1, and CH8-2 are shown by the blue, red, and green lines, respectively. The colored shaded regions denote the extent of the emission lines, as measured from the line FWHMs from the observed IMACS spectra.

(A color version of this figure is available in the online journal.)

Such halos have been predicted, but have yet to be observed at high redshift. Given the modest signal to noise of our Lyα imaging detections, it is likely that we have not detected the full extent of these halos—rather we are just seeing the tip of the iceberg, in that the Lyα light appears more extended that the rest-frame UV continuum. However, given the low signal to noise of the LAEs in our data, it is difficult to tell if we are truly seeing the edge of the Lyα emission. One way to check whether our imaging has captured all of the Lyα light is to compare the fluxes from the F658N imaging to that from ground-based photometry, which can be more sensitive to diffuse emission given the larger telescope apertures, and reduced sensitivity to read noise.

We can perform this analysis for our sample of LAEs, which have their ground-based narrowband magnitudes tabulated in Table 1 of Finkelstein et al. (2009b). These magnitudes are 24.15 ± 0.11, 24.44 ± 0.15, and 24.39 ± 0.16 for CHa-2, CH8-1, and CH8-2, respectively. Comparing these magnitudes to those of the same objects from *HST* in the F658N data, we find that all objects have significantly greater ground-based narrowband fluxes than from *HST*, with flux ratios of $f_{\mathrm{ground}}/f_{\mathrm{HST}}$ of 2.0 ± 0.6, 2.0 ± 0.5, and 1.3 ± 0.3 for these three objects, respectively.

However, both the ground- and space-based narrow bands contain both Lyα and continuum flux. We have thus used the narrowband fluxes from both ground and space, as well as the F775W flux (representing the UV continuum) along with the relevant filter curves to extract the flux in the Lyα line only (following, e.g., Malhotra & Rhoads 2002; Venemans et al. 2005). We find ratios of $f_{\mathrm{Ly}\alpha,\mathrm{ground}}/f_{\mathrm{Ly}\alpha,\mathrm{HST}} = 3.0 \pm 1.3$, 2.3 ± 0.7, and 1.5 ± 0.7 for CHa-2, CH8-1, and CH8-2, respectively.

This does not account for the position of the Lyα line in the filter. Figure 10 shows the ground-based narrowband filters used to select these three objects, as well as that of F658N on ACS. The colored vertical lines denote the position of Lyα for these

[25] One additional issue of CTE that enters in at low background is the impact of the read noise, which did not go through the charge-transfer process. We examined the corrections with and without the readnoise mitigation employed in Anderson & Bedin (2010) and found the resulting images to be essentially the same.

Table 3
Ground- versus Space-based Lyα-derived Fluxes

Object	$m_{\rm F658N}$ (mag)	$m_{\rm ground}$ (mag)	$m_{\rm F775W}$ (mag)	$f_{\nu,\rm ground}/f_{\nu,\rm F658N}$	$f_{\rm Ly\alpha,ground}/f_{\rm Ly\alpha,F658N}$
CHa-2	24.90 ± 0.28	24.15 ± 0.11	25.56 ± 0.06	2.0 ± 0.6	3.9 ± 1.7
CH8-1	25.20 ± 0.22	24.44 ± 0.15	26.54 ± 0.14	2.0 ± 0.5	8.9 ± 2.7
CH8-2	24.64 ± 0.20	24.39 ± 0.16	24.98 ± 0.04	1.3 ± 0.3	9.6 ± 4.5

Notes. A comparison of the narrowband fluxes from ground- and space-based photometry. The ground-based narrowband magnitude is from the NB656 filter for CHa-2, and from the NB665 filter for CH8-1 and CH8-2. Comparing the bandpass averaged fluxes from the narrowband images, we find that the ground-based images show a significant flux excess over the space-based images. Correcting for the continuum light in the bandpasses as well as the position of the Lyα line in the filter, we compute the ratio of Lyα fluxes from ground and space, finding an even more significant excess from the ground. This implies that there is an even more extended halo that is below the surface-brightness limit of our F658N observations, yet is still detected from the ground.

three objects, while the lighter shaded regions denote the FWHM of these lines, as measured from the IMACS spectra presented in Section 3.1. From this figure, we can see that all objects have their Lyα emission lines encompassed within the FWHM of the F658N filter. However, only CHa-2 has Lyα within the FWHM of the NB656 ground-based filter—both CH8-1 and CH8-2 were detected even though their redshift puts the emission line at $<30\%$ of the peak F665N filter transmission, thus the true flux difference between the ground- and space-based observations for these objects is larger.

To correct our flux ratios for this effect, we followed Equation (17) of Venemans et al. (2005) which folds in the position of Lyα in the filter, as well as the UV spectral slope of the object (β), which is important here as our broadband filter is redward of our narrowband filters. We used the values of the UV spectral slope computed for these objects from Finkelstein et al. (2009a), which are $\beta = -2.5$, -0.35, and -2.67 for CHa-2, CH8-1, and CH8-2, respectively. We find filter-corrected ratios of ground-based Lyα flux to space-based Lyα flux of 3.9 ± 1.7, 8.9 ± 2.7, and 9.6 ± 4.5 for Cha-2, CH8-1, and CH8-2, respectively. All three LAEs have a greater Lyα flux measured by the ground at $>2\sigma$ significance, providing further evidence that these objects have significant Lyα emission escaping in a diffuse halo, as the ground-based narrowband imaging detects up to $\sim 10\times$ more flux than *HST*. Table 3 lists the ground- and space-based magnitudes, as well as these flux ratios, for our sample. These results are consistent with those recently obtained by Steidel et al. (2011), who used extremely deep stacks of both LBGs and LAEs to study Lyα emission out to very large radii. They found that all galaxies, even LBGs with no spectroscopic Lyα emission, exhibited a large Lyα halo, and that accounting for this extended Lyα emission increases the total Lyα flux by a factor of ~ 5 on average.

We caution that as these objects are near the image depth limits in both sets of data, there could be zeropoint issues. As a test, we compared the narrowband fluxes from the ground-based NB665 image (using $2\farcs3$ aperture magnitudes from the catalog from Finkelstein et al. 2008) to the F658N data to see if there is a zeropoint offset. We examined objects in common in both catalogs, computing the mean magnitude difference in bins of 0.5 mag. From $21 < m_{\rm F658N} < 25$, the mean magnitude difference is always <0.1 mag. However, there is of course scatter in the individual objects. At bright magnitudes, this is small, with $\sigma \sim 0.3$ mag, increasing to $\sigma \sim 0.5$ mag at $m_{\rm F658N} < 25$. The magnitude differences CH8-1 is thus significant, while the magnitude difference for CH8-2 is of similar size as the 1σ uncertainty in the relative zero points. We performed a similar exercise for the shallower NB656 image, finding that the magnitude differences between objects in both NB656 and F658N were not centered around zero, but rather at a few tenths of a magnitude. However, the typical scatter in these points was ~ 0.4 mag, thus this offset is not significant. In any case, the offset is in the direction such that if real, it would make the NB656 magnitudes fainter than they truly are, strengthening our result. The F658N–NB656 color for CHa-2 is 0.75 mag, thus this object is significantly brighter in the ground-based narrow band, even when accounting for zeropoint scatter. We conclude that this flux difference is intriguing, and that a similar analysis with a larger LAE sample will provide greater confidence in this effect.

6. CONCLUSIONS

We have performed high-resolution *HST* F658N narrowband imaging over a portion of the GOODS CDF-S in order to directly image resolved Lyα emission at $z = 4.4$. We have detected Lyα emission from three spectroscopically confirmed LAEs in these data.

Studying the relative positions of these objects in their Lyα light (from the F658N data) and their rest-frame UV continuum light (from existing F775W data), we find that our data do not support a positional offset between the two types of emission. We then measured the light profiles and half-light radii from our three LAEs in both filters. We find that in two of the three objects the Lyα light profile rises more slowly, and in one object the Lyα light has a significantly larger half-light radius than the rest-frame UV continuum emission. We confirmed this result by stacking the galaxy images in both bands, finding that the Lyα emission has $r_h = 1.1$ kpc, while the rest-frame UV continuum is more compact with $r_h = 0.7$ kpc. This implies that the Lyα light is more spread out, presumably due to effects of resonant scattering, possibly in a clumpy ISM.

To investigate this further, we compared the fluxes of our LAEs in the F658N narrow band to ground-based narrowband measurements, which are more sensitive to diffuse emission due to, among other things, larger telescope apertures. We find that in all three cases where we have measurements from both ground and space, the ground-based narrowband fluxes are significantly ($>2\sigma$) greater than the space-based fluxes, by factors of $\sim$4–10. This shows that the larger physical sizes detected in the F658N data are only the tip of the Lyα iceberg, and that the majority of the Lyα emission may lie in a larger, diffuse halo. It is thus clearly important to include the ISM geometry and kinematics in any study of Lyα emission at high redshift. This is consistent

with recent theoretical results, which show that all star-forming galaxies should exhibit these diffuse halos, and observational results of Lyα blobs, which imply a continuous distribution of Lyα sizes, from point-like out to extended blobs.

While Lyα emission is one of the most powerful tools we have to discover and study galaxies at high redshift, the complicated radiative transfer undergone by Lyα photons in their host galaxies muddle the physics that can be inferred. In order to maximize our understanding of LAEs and Lyα emission in general, we need to obtain a greater understanding of how Lyα makes its way from the H II regions where it originates to its point of escape from the galaxy. Studying the Lyα spatial profiles provides one estimate of the complex radiative transfer by comparing the Lyα morphologies to those of the rest-frame UV, but more work is needed to obtain strong detections of these diffuse halos, which likely requires the next generation of ground- and space-based observatories.

We are grateful to the men and women who worked tirelessly for many years to make Wide Field Camera 3 the instrument it is today, and to the STScI Director M. Mountain for the discretionary time to make this program possible. Support for *HST* program 11359 was provided by NASA through grants GO-11359.0.A from the Space Telescope Science Institute, which is operated by the Association of Universities for Research in Astronomy, Inc., under NASA contract NAS 5-26555. We thank the astronauts of STS-125 to *HST* for risking their lives to bring us a new and improved world class observatory. Their hard work and dedication is greatly appreciated. S.L.F. and K.D.F. are supported by the Texas A&M Department of Physics and Astronomy. The work of S.M. and J.E.R. is supported by the National Science Foundation grant AST-0808165.

REFERENCES

Anderson, J., & Bedin, L. R. 2010, PASP, 122, 1035
Bertin, E., & Arnouts, S. 1996, A&AS, 117, 393
Bielby, R., et al. 2010, arXiv:1005.3028
Bond, N. A., Feldmeier, J. J., Matković, A., Gronwall, C., Ciardullo, R., & Gawiser, E. 2010, ApJ, 716, L200
Bond, N. A., Gawiser, E., Gronwall, C., Ciardullo, R., Altmann, M., & Schawinski, K. 2009, ApJ, 705, 639
Capak, P., et al. 2008, ApJ, 681, L53
Ferguson, H. C., et al. 2004, ApJ, 600, L107
Finkelstein, S. L., Malhotra, S., Rhoads, J. E., Hathi, N. P., & Pirzkal, N. 2009a, MNRAS, 393, 1174
Finkelstein, S. L., Rhoads, J. E., Malhotra, S., & Grogin, N. 2009b, ApJ, 691, 465
Finkelstein, S. L., Rhoads, J. E., Malhotra, S., Grogin, N., & Wang, J. 2008, ApJ, 678, 655
Finkelstein, S. L., Rhoads, J. E., Malhotra, S., Pirzkal, N., & Wang, J. 2007, ApJ, 660, 1023
Finkelstein, S. L., et al. 2011, ApJ, 729, 140
Gawiser, E., et al. 2006, ApJ, 642, L13
Gronwall, C., Bond, N. A., Ciardullo, R., Gawiser, E., Altmann, M., Blanc, G. A., & Feldmeier, J. J. 2010, arXiv:1005.3006
Hansen, M., & Oh, S. P. 2006, MNRAS, 367, 979
Hathi, N. P., Jansen, R. A., Windhorst, R. A., Cohen, S. H., Keel, W. C., Corbin, M. R., & Ryan, R. E., Jr. 2008a, AJ, 135, 156
Hathi, N. P., Malhotra, S., & Rhoads, J. E. 2008b, ApJ, 673, 686
Koekemoer, A. M., Fruchter, A. S., Hook, R. N., & Hack, W. 2002, in The 2002 HST Calibration Workshop: Hubble After the Installation of the ACS and the NICMOS Cooling System, ed. S. Arribas, A. Koekemoer, & B. Whitmore (Baltimore, MD: STScI), 337
Komatsu, E., et al. 2011, ApJS, 192, 18
Kudritzki, R., et al. 2000, ApJ, 536, 19
Lai, K., Huang, J.-S., Fazio, G., Cowie, L. L., Hu, E. M., & Kakazu, Y. 2007, ApJ, 655, 704
Malhotra, S., & Rhoads, J. E. 2002, ApJ, 565, L71
Malhotra, S., Rhoads, J. E., Finkelstein, S. L., Hathi, N., Nilsson, K., McLinden, E., & Pirzkal, N. 2011, ApJL, submitted
McLinden, E. M., et al. 2010, ApJ, submitted (arXiv:1006.1895)
Neufeld, D. A. 1991, ApJ, 370, L85
Nilsson, K. K., & Møller, P. 2009, A&A, 508, L21
Nilsson, K. K., Tapken, C., Møller, P., Freudling, W., Fynbo, J. P. U., Meisenheimer, K., Laursen, P., & Östlin, G. 2009, A&A, 498, 13
Nonino, M., et al. 2009, ApJS, 183, 244
Oesch, P. A., et al. 2010, ApJ, 709, L21
Ono, Y., et al. 2010, MNRAS, 402, 1580
Östlin, G., Hayes, M., Kunth, D., Mas-Hesse, J. M., Leitherer, C., Petrosian, A., & Atek, H. 2009, AJ, 138, 923
Partridge, R. B., & Peebles, P. J. E. 1967, ApJ, 147, 868
Pentericci, L., Grazian, A., Fontana, A., Castellano, M., Giallongo, E., Salimbeni, S., & Santini, P. 2009, A&A, 494, 553
Pirzkal, N., Malhotra, S., Rhoads, J. E., & Xu, C. 2007, ApJ, 667, 49
Retzlaff, J., Rosati, P., Dickinson, M., Vandame, B., Rité, C., Nonino, M., Cesarsky, C., & GOODS Team. 2010, A&A, 511, A50
Rhoads, J. E., et al. 2009, ApJ, 697, 942
Shapley, A. E., Steidel, C. C., Pettini, M., & Adelberger, K. L. 2003, ApJ, 588, 65
Steidel, C. C., Bogosavljević, M., Shapley, A. E., Kollmeier, J. A., Reddy, N. A., Erb, D. K., & Pettini, M. 2011, arXiv:1101.2204
Venemans, B. P., et al. 2005, A&A, 431, 793
Waddington, I., Windhorst, R. A., Cohen, S. H., Partridge, R. B., Spinrad, H., & Stern, D. 1999, ApJ, 526, L77
Windhorst, R. A., Keel, W. C., & Pascarelle, S. M. 1998, ApJ, 494, L27
Windhorst, R. A., et al. 2011, ApJS, 193, 27
Yang, Y., Zabludoff, A., Eisenstein, D., & Davé, R. 2010, ApJ, 719, 1654
Zheng, Z., Cen, R., Trac, H., & Miralda-Escudé, J. 2010, ApJ, 716, 574